

Lessons learned from NASA’s DART impact about disrupting rubble-pile asteroids

S. D. Raducan¹, M. Jutzi¹, C. C. Merrill², P. Michel^{3,4}, Y. Zhang⁵, M. Hirabayashi⁶, and A. Mainzer⁷

¹Space Research and Planetary Sciences, Physikalisches Institut, University of Bern, Bern, Switzerland

²Sibley School of Mechanical and Aerospace Engineering, Cornell University, Ithaca, NY, USA

³Université Côte d’Azur, Observatoire de la Côte d’Azur, CNRS, Laboratoire Lagrange, Nice, France

⁴The University of Tokyo, Department of Systems Innovation, School of Engineering, Tokyo, Japan

⁵Department of Climate and Space Sciences and Engineering, University of Michigan, Ann Arbor, MI 48109, USA

⁶Georgia Institute of Technology, Atlanta, GA, USA

⁷University of Arizona, Lunar and Planetary Laboratory, Tucson, AZ, USA

Abstract

We present a series of numerical simulations using a shock physics smoothed particle hydrodynamics (SPH) code, investigating energetic impacts on small celestial bodies characterised by diverse internal structures, ranging from weak and homogeneous compositions to rubble-pile structures with varying boulder volume packing. Our findings reveal that the internal structure of these rubble-pile bodies significantly influences the impact outcomes. Specifically, we observe that the same impact energy can either catastrophically disrupt a target with a low boulder packing ($\lesssim 30$ vol%), or result in the ejection of only a small fraction of material from a target with the same mass but high boulder packing ($\gtrsim 40$ vol%). This finding highlights the pivotal role played by the rubble-pile structure, effectively acting as a bulk shear strength, which governs the size and behaviour of the resulting impact. Consequently, understanding and characterising the internal structure of asteroids will be of paramount importance for any future efforts to deflect or disrupt an asteroid on a collision course with Earth.

1 Introduction

In a significant milestone for human history, NASA’s DART (Double Asteroid Redirection Test) spacecraft impacted the asteroid Dimorphos, the secondary of the Didymos asteroid binary system, on September 26th, 2022 (UTC) (Chabot et al., 2023; Daly et al., 2023; Rivkin et al., 2021). The impact resulted in an orbital change of approximately 33 minutes of Dimorphos around its primary, Didymos (Thomas et al., 2023). This groundbreaking achievement demonstrated the capability to redirect the trajectory of a potentially hazardous asteroid, paving the way for future efforts to protect our planet from potential threats. The DART spacecraft with a mass of 580 kg collided with Dimorphos at 6.15 km/s, hitting the target within 25 m of the centre of figure of the asteroid and at an incidence angle of only $16.7 \pm 7.4^\circ$ from the average surface normal. This angle was calculated based on a 1.5-meter radius around the impact point, using data from the global digital terrain model (DTM) of the impact site (Daly et al., 2023).

Dimorphos is an oblate ellipsoid, with $\approx 87.90 \times 86.96 \times 57.16$ m (Daly et al., 2023), having an equivalent volume of a ≈ 150 m sphere. ESA’s Hera mission will visit the Didymos binary system in late 2026 for rendezvous investigations.

To date, we have discovered more than 32,000 objects in the Near-Earth Object (NEO) population¹. Only approximately one-third of these objects exceed a size of 140 meters. However, it is noteworthy that less than half of the asteroids falling within the size range of 20 to 140 meters have been located to date (Harris & Chodas, 2021), many of which are not well catalogued. The prediction is that the impact frequency of objects in this size range is higher due to the increasing number of smaller objects. Ongoing initiatives are underway to identify and monitor asteroids within this critical size range. This casts the significance of better characterising how such small asteroids contribute to the hazards on the Earth.

To put it into perspective, consider the Chelyabinsk event in February 2013 (Popova et al., 2013). This incident involved a relatively small asteroid, approximately 20 meters in diameter (Artemieva & Shuvalov, 2016), which entered Earth’s atmosphere and exploded at an altitude of 27 km near Chelyabinsk, Russia. Despite its modest size, the explosion caused extensive damage, primarily to buildings in the area due to shock wave propagation. The only other large meteoroid airburst recorded in the last century occurred on June 30th, 1908 over the Tunguska forest in Siberia (Russia). The Tunguska event produced even more extensive damage, flattening approximately 2000 square km of forest (Artemieva & Shuvalov, 2016). The event is believed to have been caused by a 30 to 50 m diameter asteroid (Artemieva & Shuvalov, 2016) that exploded 6-10 km in the atmosphere.

Upon detecting a potentially hazardous asteroid heading toward Earth, the immediate priority lies in determining our course of action. This pivotal decision relies on a thorough analysis of the asteroid’s size, composition, and trajectory (e.g., Rumpf et al., 2020). Different asteroids may require different techniques and energies to deflect them, and a deflection strategy is usually favoured over disruption, where at least half of the target’s original mass is ejected and leads to the creation of a cloud of potentially hazardous fragments with uncertain size.

With DART’s success, we now know that a kinetic impactor is a viable option to deflect a potentially hazardous asteroid, as long as we do it long enough in advance. But the DART mission was just the first kinetic impactor test, and missions to impact bodies smaller than Dimorphos are being designed (e.g., Merrill et al., 2024) and planned with launch dates even as early as 2025 (e.g., Wang et al., 2023). However, deflection missions require detailed planning, and we need to be able to answer the question “What is the smallest asteroid size that is feasible to be deflected by a kinetic impactor, without disrupting it?”. Here, we use numerical models of asteroid impacts to address this question. We leverage the invaluable data from the DART impact and extrapolate it to rubble-pile asteroids of different sizes.

2 Insights gained from the DART impact about the mechanical properties of Dimorphos

Prior to the impact, there was a large uncertainty regarding the mechanical properties of both Didymos and Dimorphos, particularly concerning their structure and surface cohesion (Raducan et al., 2020; Raducan et al., 2019; Stickle et al., 2022). Geological assessment of the two asteroids, based on images captured by the onboard DRACO camera during the DART approach, suggests that both asteroids are rubble-pile objects (Barnouin et al., 2023), i.e., accumulations of debris held together primarily by self-gravity and/or small cohesive forces (Richardson et al., 2022; Scheeres et al., 2010; Walsh et al., 2008). Barnouin et al. (2023) concluded that the surface of Dimorphos has a cohesion of at most 0.03 Pa and estimated a friction angle of 35 degrees, however, a stiffer interior is not excluded.

These results are also supported by numerical simulations of the DART impact outcome. Raducan et al. (2023) compared simulation results from an extensive set of runs, systematically varying the mechanical properties of the target (e.g., interparticle cohesion, coefficient of internal friction, bulk porosity) and the boulder size-frequency distribution (SFD), with the observed deflection efficiency (Cheng et al., 2023), the shape and morphology of the ejecta cone (Dotto et al., 2023; Li et al., 2023), and the estimated amount of ejecta mass (Graykowski et al., 2023). They found that in

¹NEA discovery statistics as of September 2023 (cneos.jpl.nasa.gov).

order to reproduce all the observables, Dimorphos must be a rubble pile, with little or no surface cohesion ($Y < a$ few Pa) and a low packing of boulders on the surface. A low boulder packing is defined as less than $\approx 30\%$ of the volume occupied by boulders larger than 2.5 m. Based on boulder SFD and boulder shape (Robin et al., 2023), they also estimate that the surface macroporosity is about 35%.

Numerical predictions of the DART impact outcome (Raducan et al., 2023) together with observations of the secondary lightcurve deduced from high-quality photometric observations [Pravec et al., in prep.] strongly suggest that the DART impact occurred in the subcatastrophic impact regime (i.e., a regime between cratering and catastrophic disruption) and that the impact caused significant reshaping of Dimorphos, as opposed to an impact crater (Raducan & Jutzi, 2022; Raducan et al., 2022). The models suggest a change in the a_s/b_s ratio of the ellipsoidal axes from 1.06 (Daly et al., 2023) to up to 1.2 (Raducan et al., 2023), while observations suggest $a_s/b_s \approx 1.3 \pm 0.1$, if the body is currently in or close to a tidally locked state with minimal libration amplitude and an approximately zero obliquity [Pravec et al., in prep.].

The ESA’s Hera mission will investigate the Didymos system in early 2027 (Michel et al., 2022) and will allow us to measure in detail the DART impact outcome, i.e., the crater’s size or global reshaping of Dimorphos, as well as Dimorphos’ internal properties, offering complete documentation of the DART impact experiment for impact code validation.

3 Previous studies

The catastrophic disruption threshold, Q_D^* , is the specific impact energy required to disperse half of the initial target mass. Historically, this threshold has been estimated through laboratory and numerical hydrocode experiments. While these methods have been valuable, they face limitations when applied to small bodies in the 10–100 m range, where the intricate interplay of material strength, friction, porosity, and self-gravitation governs outcomes. Laboratory experiments become impractical at this scale, leading to the increased use of numerical approaches. For example, Benz & Asphaug (1999) employed a smoothed particle hydrodynamics (SPH) code to model the fracturing of basalt and icy bodies. They integrated a tensile fragmentation model but did not account for target porosity or heterogeneities. Leinhardt & Stewart (2009) used the CTH code (McGlaun et al., 1990) to study the dependence of Q_D^* on the limiting yield strength of the target, focusing on homogeneous solid objects. In Jutzi et al. (2010), the effects of target microporosity on Q_D^* was explored using a sub-resolution porosity model ($P - \alpha$ model) (Jutzi et al., 2008). Subsequent studies by Jutzi (2015) and Arakawa et al. (2022) also explored the effects of target friction and cohesion, employing a combination of laboratory experiments and numerical simulations.

Most of the previous studies used internally homogeneous objects. Benavidez et al. (2018); Benavidez et al. (2012) investigated collisions among “rubble-pile” bodies using the SPH code by Benz & Asphaug (1994,9). However, these simulations did not account for friction between the boulders/grains, leading to significantly low Q_D^* , as discussed in Jutzi (2015). The collisional strength of small (10 – 100 m) rubble-pile asteroids has yet to be systematically studied using realistic material properties, and recent work showed that the presence of macroscopic boulders has a large influence on the impact response of these objects (Raducan et al., 2022). The novelty of the work presented in this study lies in its use of material models and parameters calibrated to an actual asteroid impact, marking the first instance of such an approach. We have used the DART impact experiment on asteroid Dimorphos to determine the optimal material models and simulation parameters for the Bern SPH code, including material strength, porosity, and boulder configuration.

4 Numerical models

We use the Bern smoothed particle hydrodynamics (SPH) impact code (Benz & Asphaug, 1995; Jutzi, 2015; Jutzi et al., 2008), to numerically model impacts of varying specific energies, over a range of assumed sets of material properties

and interior structures for the target. From our simulations, we compute the size of the largest remnant and compute the catastrophic disruption threshold, Q_D^* .

Bern SPH is a shock physics code originally developed by Benz & Asphaug (1994,9) to model the collisional fragmentation of rocky bodies and was later parallelised (Nyffeler, 2004) and further extended by (Jutzi et al., 2008) and (Jutzi, 2015) to model porous and granular materials. The most recent version of the code includes a tensile fracture model (Benz & Asphaug, 1995), a porosity model based on the $P - \alpha$ model (Jutzi et al., 2008), pressure-dependent strength models (Jutzi, 2015), and self gravity. The Bern SPH code has been validated in a number of studies (e.g., Jutzi, 2015; Jutzi et al., 2009; Ormö et al., 2022) and benchmarks against other codes (e.g., Luther et al., 2022).

4.1 Rubble-pile models

We model kinetic impacts into rubble-pile ellipsoidal targets composed of spherical boulders with different distributions embedded into a matrix material. We used the N-body code pkdgrav (Richardson et al., 2000) to generate rubble-pile targets, and we used Dimorphos’ surface boulder size-frequency distribution (SFD) (Pajola et al., 2023) to generate boulder dimensions. To explore a large possible range of boulder mass fractions, we removed some of these boulders from pkdgrav output when we built our SPH models. In addition to a homogeneous target scenario (0 vol%; Fig. 1a), we define four different boulder distributions, with $\approx 20, 30, 40$ and 50% of the target volume occupied by boulders (Fig. 1). Boulders smaller than $R_{min} = 1.25$ m (2.5 m in diameter) are removed from the SFD due to their size being too small to be resolved individually (Fig. 1c). We assume they are part of the matrix material used to fill the voids between the larger boulders. From the initial pkdgrav boulder re-accumulation, we cut out oblate ellipsoidal targets with three different sizes: a) $87.90 \times 86.96 \times 57.16$ m, corresponding to Dimorphos’s shape from Daly et al. (2023); b) $58.60 \times 57.97 \times 38.11$ m ($\approx 35\%$ smaller than Dimorphos); and c) $29.30 \times 28.99 \times 19.05$ m ($\approx 65\%$ smaller than Dimorphos). Our targets have volume-equivalent diameters of ≈ 150 m ($R \approx 75$ m), ≈ 100 m ($R \approx 50$ m), and ≈ 50 m ($R \approx 25$ m). When we constructed our targets, we aimed to keep a similar target mass for a specific target size, irrespective of boulder packing. Consequently, the target mass for each size varies by only approximately 10% with different boulder packing densities.

4.2 Material model

To model the rubble piles, we assigned material properties that Raducan et al. (2023) and Barnouin et al. (2023) found to be the best fit for the surface mechanical properties of Dimorphos. We modelled both the boulders and the matrix material using the Tillotson equation of state (EoS) for basalt, with modified initial grain densities of $\rho_g = 3200$ kg/m³. The bulk porosity of Dimorphos results from a combination of macroporosity found between individual boulders, as well as microporosity within the boulders themselves. Based on analysis of the reflectance spectra of Didymos, the best matching meteorite analogues are the L/LL ordinary chondrites (de León et al., 2006; Dunn et al., 2013; Ieva et al., 2022). These meteorites have grain densities of ≈ 3200 – 3600 kg/m³, and low microporosities of ≈ 8 – 10% (Flynn et al., 2018). Therefore, in our simulations, the initial microporosity within boulders was fixed at 10% . The initial porosity of the matrix (macroporosity + microporosity) was fixed at 45% , as calculated by (Raducan et al., 2023). The porosity in both the boulders and the matrix was modelled using the $P - \alpha$ porosity compaction model (Jutzi et al., 2008), with a single power-law slope, defined by the solid pressure, P_s , elastic pressure, P_e , exponent, n , and initial distension, α_0 :

$$\alpha(P) = \begin{cases} 1, & \text{if } P_s < P \\ (\alpha_0 - 1) \left(\frac{P_s - P}{P_s - P_e} \right)^n + 1, & \text{otherwise.} \end{cases} \quad (1)$$

The input parameters for the matrix and boulder materials are summarised in Table 1.

In all of our simulations, the boulders, which are represented explicitly, are modelled using a tensile strength and fracture model as described in (Jutzi, 2015; Jutzi et al., 2008), with parameters corresponding to a tensile strength of

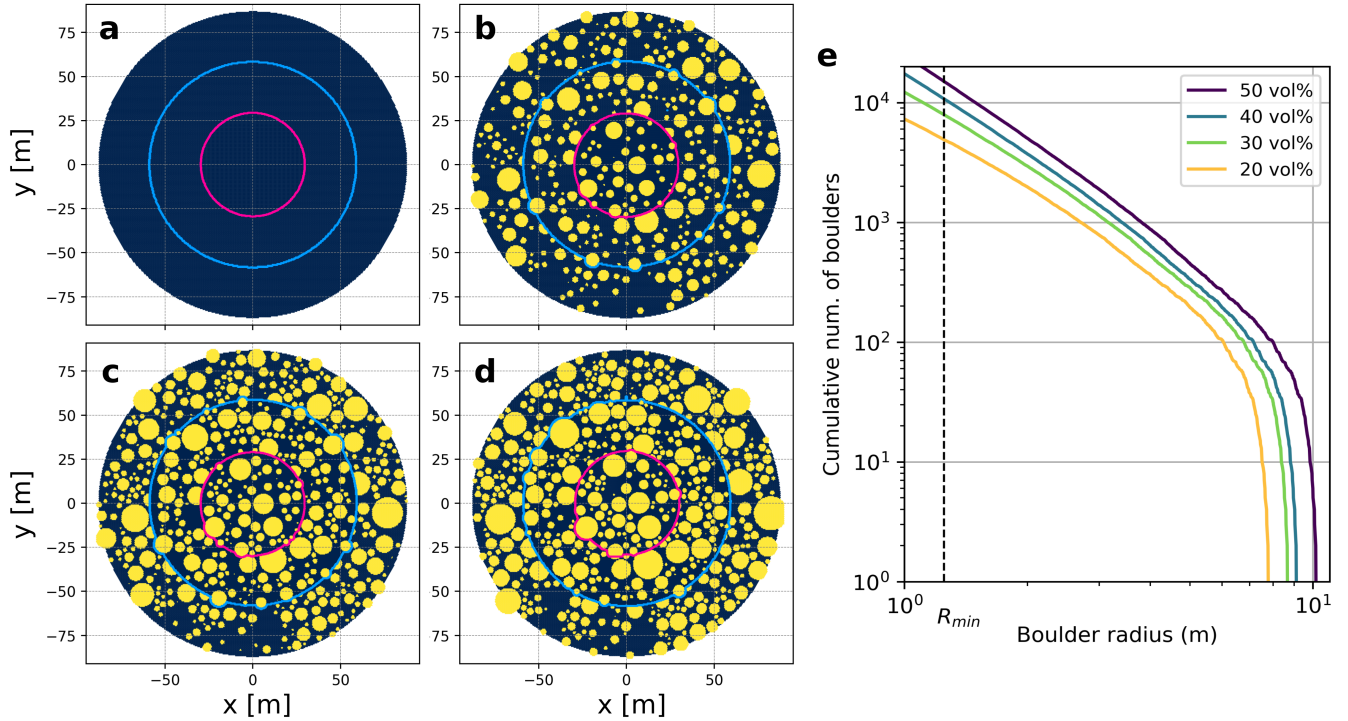


Figure 1: Cross-sections through the targets used in the SPH simulations, with different boulder packings: a) 0 vol%, b) 30 vol%, c) 40 vol% and d) 50 vol %. In each panel, the outlines show the three target sizes simulated: $87.90 \times 86.96 \times 57.16$ m; $58.60 \times 57.97 \times 38.11$ m; and $29.30 \times 28.99 \times 19.05$ m. In all simulations, the impact is vertical, along the y axis. e) Boulder size-frequency distributions (SFD) for each boulder packing studied here. The 20 vol% packing SFD is plotted for comparison. Due to resolution constraints, boulders smaller than $R_{\min} = 2.5$ m are not explicitly modelled; instead, they are included in the matrix material and treated as a continuum.

$Y_T = 10$ MPa. While the individual boulders possess significant strength, the inter-particle cohesion is considered to be negligible ($Y_0 \approx 0$ Pa) (Barnouin et al., 2023). We model this matrix material using a simple pressure-dependent strength model (Collins et al., 2004; Lundborg, 1967), in which the strength asymptotes to a certain shear strength at high pressures. For $Y_0 = 0$ Pa, the Lundborg (LUND) strength model describes the yield strength as:

$$Y = \frac{fP}{1 + fP/(Y_{dm})} \quad (2)$$

where P is pressure, f is the coefficient of internal friction, and Y_{dm} is the limiting strength at high pressure.

The projectile was modelled as an underdense (1000 kg/m^3) aluminium sphere and the impact velocity was kept constant at 6 km/s. The projectile hit the target at $x = 0$, along the y -direction (Fig. 1). We investigate two impact angles: vertical (0° from the surface normal) and oblique, 45° impact angle. To vary the specific impact energy, we vary the mass of the projectile between 200 kg and 5×10^5 kg.

Table 1: Material model parameters for impact simulations into Dimorphos analogues.

Description	Impactor	Matrix material	Boulders
Material	Aluminium	Basalt	Basalt
Equation of state	Tillotson ^a	Tillotson ^b	Tillotson ^b
Initial bulk modulus, A (GPa)	7.5	26.7	26.7
Fast-integration bulk modulus (MPa)	1.0	1.0	1.0
Grain density, ρ_g (kg/m ³)	1000	3200	3200
Strength model	von Mises	LUND ^c	LUND ^c
LUND strength parameters ^c			
Damage strength at zero pressure, Y_0 (Pa)	–	0	1×10^8
Strength at infinite pressure, Y_{dm} (GPa)	0.34	3.5	3.5
Internal friction coefficient (damaged), f	–	0.55	0.8
Porosity model parameters ($P - \alpha$) ^d			
Initial porosity, ϕ_0	–	45%	10%
Initial distension, α_0	–	1.80	1.15
P_s (GPa)	–	1.0	2.0
P_e (MPa)	–	1.0	1.0
n	–	2	2

^aTillotson (1962); ^bBenz & Asphaug (1999); ^cLundborg (1967); ^dJutzi et al. (2008).

The simulations were ran until $T = 500$ seconds after the impact. To model these late times, after 15 seconds, we switch to a “fast integration scheme”, as described in Jutzi et al. (2022); Raducan & Jutzi (2022). At this time, the initial shock and fragmentation phase are over, and the late-stage evolution is governed by low-velocity granular flow. This allows us to artificially change the material properties of the target to a low sound-speed medium, allowing for a larger timestep. In this calculation phase, we apply a simplified Tillotson equation of state (EoS) for all materials, in which all energy-related terms are set to zero. The remaining leading term of the EoS is governed by the bulk modulus, given by $P = A(\rho/\rho_0 - 1)$, which also determines the magnitude of the sound speed. We use $A \approx 1$ MPa and also reduce the shear modulus proportionally.

4.3 Largest remnant calculations

In the collisional disruptions at the scales investigated here, the largest remnant is the accumulation of an array of gravitationally bound materials (i.e., intact monolithic fragments, re-accumulated dust, etc.). To quantify the mass of the largest remnant formed by the reaccumulation process of the smaller pieces, we use a “fragment search” iterative procedure introduced in Benz & Asphaug (1999).

This method identifies gravitationally bound aggregates by calculating the binding energy of all particles and fragments relative to either the largest intact fragment or, if too small, the particle closest to the potential minimum. Initially, this seed particle marks the nucleation point for the total bound mass. Unbound particles are removed, and the centre of mass position and velocity of the aggregate are computed. The process is repeated, recalculating the binding energy for the remaining fragments and particles relative to this new position and velocity, with unbound particles discarded at each iteration. Typically, convergence occurs within a few iterations, with few particles lost after the initial 2-3 steps. Finally, the method verifies that the members of this gravitationally bound aggregate are close spatially, using a friends-of-friends algorithm. Information such as mass, position, velocity, angular momentum, and moment of inertia is determined for this aggregate, consisting of smaller fragments and individual particles.

This method was shown to be accurate in determining the largest reaccumulated fragment (M_{lr}), as long as it has a significant size ($M_{lr}/M_{tot} > 10\text{-}20\%$) (Jutzi et al., 2010), where M_{tot} is the total initial mass of the asteroid (Jutzi et al., 2010).

5 Results

5.1 Effects of the boulder packing

We find that the interior structure of the rubble-pile asteroid plays a significant role in the outcome of the impact. Figure 2 shows the simulations outcome from a $M_p \approx 2.6 \times 10^4$ kg ($R_p = 1.84$ m) impactor hitting four Dimorphos-like ellipsoidal targets ($87.90 \times 86.96 \times 57.16$ m), at 6 km/s. The boulder packing (i.e., volume occupied by large, >2.5 m, boulders) increases from left (homogeneous; 0 vol%) to right (50 vol%). For all target scenarios, the initial target mass is $4.15 \times 10^9 \pm 5\%$ kg.

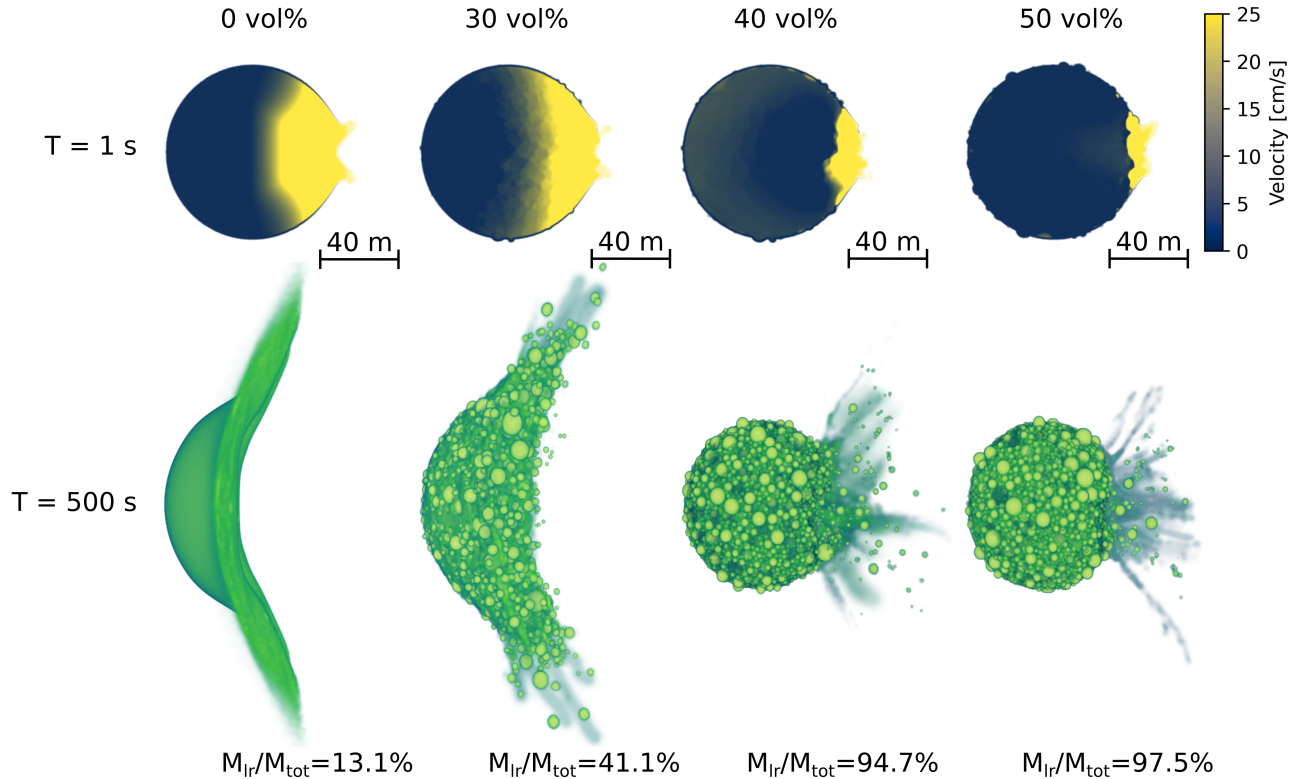


Figure 2: Bern SPH simulations of collisions between a $87.90 \times 86.96 \times 57.16$ m target and impactor of $R_p = 1.84$ m ($M_p = 2.6 \times 10^4$ kg), with a relative velocity of 6 km/s and a vertical impact angle. Targets with four different packing (0–50 vol%) are investigated. (top row) Cross-section of SPH simulations showing the velocity field in the target at $T = 1$ s. (bottom row) SPH simulations show the degree of disruption at $T = 500$ s and the size of the largest remnant (M_{lr}).

The upper row in Figure 2 displays cross-sections of the four SPH simulations, showing the magnitude of the velocity field, at $T = 1$ second after the impact. With increasing boulder packing, the pressure generated by shock wave propagation is attenuated by the presence of the boulders. In targets with higher boulder packing, a greater amount of energy is dissipated in the process of disrupting the boulders near the impact site, and the interlocking of boulders further hinders the shear motion of materials. Consequently, this leads to lower overall particle velocities within the target. This, in turn, results in less material being excavated by the impact and escaping the body’s gravitational field. The largest remnant from impacting a $M_p = 2.6 \times 10^4$ kg projectile on these rubble-pile targets with an initial mass, $M_{tot} \approx 4.15 \times 10^9 \pm 5\%$ kg, is $M_{lr} = 13.1\%$ of M_{tot} for a homogeneous structure, $M_{lr} = 41.1\%$ for a target with 30 vol% and $M_{lr} = 94.7\%$ and $M_{lr} = 97.5\%$ for 40 vol% and 50 vol%, respectively (Fig. 2, bottom panels). This means that the same impact would excavate only a few percent of the target mass if the boulder packing is larger than about 40%, but catastrophically disrupt the targets with lower boulder packing ($\lesssim 30$ vol%).

5.2 Catastrophic disruption threshold for vertical and oblique impacts

From our simulations of vertical impacts into ≈ 150 m targets at 6 km/s, we find that with increasing boulder packing, an increasing amount of impact energy per unit mass is required to catastrophically disrupt the target (i.e., eject half of the initial mass). We find $Q_D^* = 80 \pm 9$ J/kg for a homogeneous target, $Q_D^* = 145 \pm 21$ J/kg for a 30 vol% target, $Q_D^* = 357 \pm 25$ J/kg for a 40 vol% target and $Q_D^* = 1136 \pm 11$ J/kg for a 50 vol% target. Similar trends are obtained for the ≈ 100 m and ≈ 50 m ellipsoidal targets. Fig. 3a shows the specific impact energy required for a catastrophic disruption, per unit mass, Q , as a function of target radius from our SPH simulations.

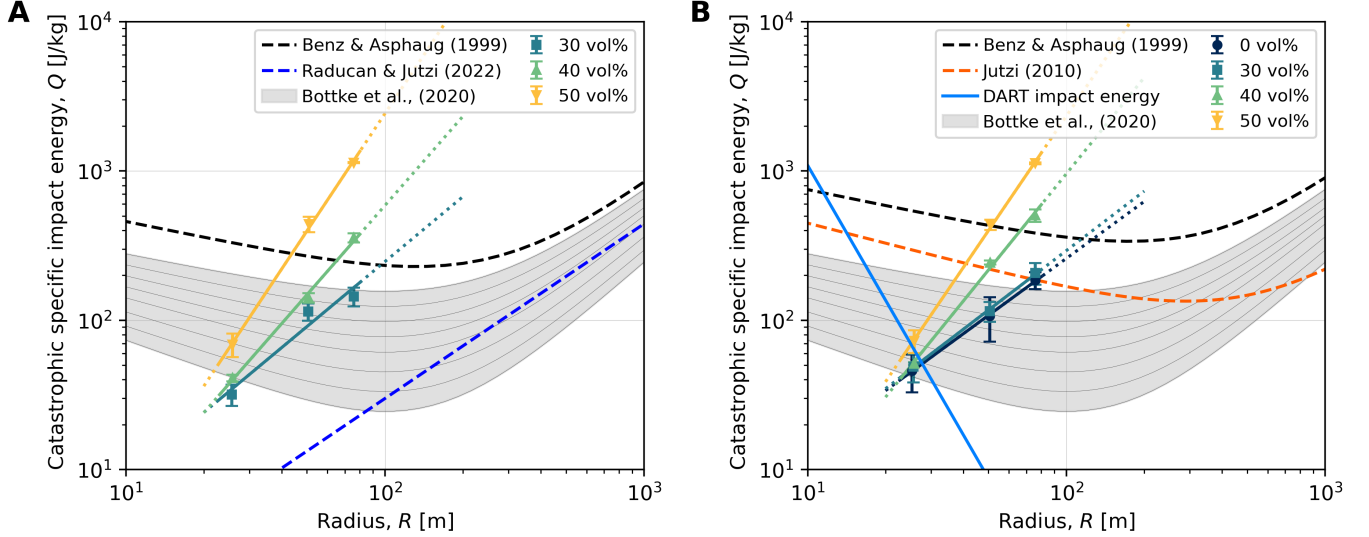


Figure 3: Specific impact energy required for a catastrophic disruption per unit mass, Q , as a function of target radius, R , for targets with different boulder packing (0 vol% to 50 vol%). A) Vertical impact and B) Oblique, 45° impact. The impact location is the same for both impact angles (see the Numerical Methods section). The DART impact energy is plotted in both A and B. Results from Benz & Asphaug (1999); Jutzi et al. (2010); Raducan & Jutzi (2022) are plotted for comparison for the respective impact angle. Q_D^* curves used by Bottke et al. (2020) are impact angle independent and are plotted in both A and B.

In the gravity regime, when the gravitational force of the target dominates over the tensile strength of the body, Q increases with target size, R , and impact velocity, U , as described by the scaling relationship (Housen & Holsapple, 1990),

$$Q = a_g R^{3\mu_g} U^{2-3\mu_g}, \quad (3)$$

where a_g is a constant, and μ_g is the coupling parameter to the target in the gravity regime. Using a best-fit algorithm, we find a_g and μ_g (Table 2). The values for targets with a boulder packing lower than 30 vol% have values comparable with what is generally assumed for typical porous materials ($\mu_g = 0.40$ – 0.42 , (Jutzi et al., 2017); $\mu_g = 0.33$ – 0.36 , (Ballouz et al., 2020)). However, the derived μ_g for >30 vol% exceeds these values, indicating other effects (boulder interlocking) are becoming more and more relevant with increasing boulder packing.

Our results show that in the size range studied here (up to $R \approx 100$ m), small rubble-pile asteroids with a low boulder packing ($\lesssim 30$ vol%) are much easier to disrupt than monolithic bodies (Benz & Asphaug, 1999; Jutzi et al., 2010). $R \approx 50$ m with low boulder packing targets have a catastrophic impact energy (Q) about 4 times smaller than derived by (Benz & Asphaug, 1999) for monolithic targets, while a $R \approx 25$ m has a Q about 20 times smaller than a monolithic target (Benz & Asphaug, 1999).

Asteroids with high packing of boulder also have smaller Q at small sizes ($R \lesssim 40$ m), but are much more resistant to impacts at $R \gtrsim 80$ m. To disrupt $R \gtrsim 80$ m targets, about 3.5 times more energy is required than to disrupt monolithic targets in the same size range (Benz & Asphaug, 1999). There are several contributing factors to

Table 2: Constants obtained from SPH simulations for catastrophic disruption threshold scaling relationships (Housen & Holsapple, 1990).

Boulder packing	90° impact		45° impact	
	a_g	μ_g	a_g	μ_g
0 vol%	$(2.15 \pm 0.33) \times 10^{-4}$	0.34 ± 0.10	$(1.29 \pm 0.12) \times 10^{-3}$	0.42 ± 0.01
30 vol%	$(2.55 \pm 0.43) \times 10^{-3}$	0.48 ± 0.12	$(1.83 \times 0.18) \times 10^{-3}$	0.44 ± 0.02
40 vol%	$(5.52 \pm 0.38) \times 10^{-2}$	0.66 ± 0.04	$(1.17 \times 0.11) \times 10^{-1}$	0.71 ± 0.04
50 vol%	2.96 ± 1.37	0.87 ± 0.03	2.17 ± 0.73	0.84 ± 0.02

these results. Firstly, the relatively high porosity (45%) of the target attenuates the shock wave in comparison to a low-porosity monolithic target. At the same time, the interlocking of boulders inhibits shear motion, consequently diminishing the impact-induced velocity gradients within the target.

In contrast to the homogeneous and cohesionless targets studied in Raducan & Jutzi (2022), the rubble-pile targets studied here are harder to catastrophically disrupt. This can be attributed to the distinct material mechanical properties considered, particularly the initial porosity, grain density, and bulk modulus of the target material.

The same trends observed for vertical impacts are also observed for oblique, 45°, impacts. We find $Q_D^* = 185 \pm 24$ J/kg for a homogeneous target, $Q_D^* = 207 \pm 34$ J/kg for a 30 vol% target, $Q_D^* = 504 \pm 50$ J/kg for a 40 vol% target and $Q_D^* = 1125 \pm 15$ J/kg for a 50 vol% target (Fig. 2). The best-fit a_g and μ_g constants for Eq. 3 are summarised in Table 2.

Once more, in cases of high boulder packing, the slope of Q (Eq. 3) is notably steeper than what has been observed in monolithic and homogeneous targets (Benz & Asphaug, 1999; Jutzi et al., 2010). This indicates that also in the case of oblique impacts, small targets (with $R \lesssim 40$ m) are more prone to catastrophic disruption than previously anticipated, whereas larger targets ($R \gtrsim 80$ m) demonstrate greater resilience to impacts.

6 Discussion

6.1 Deflection vs. disruption

A catastrophic disruption event reduces the target to less than half of its original mass (e.g., Holsapple & Housen, 2019) and leads to the creation of a cloud of potentially hazardous fragments from the ejecta. The trajectories of these fragments are highly sensitive to unpredictable variables, such as the asteroid’s internal structure, introducing uncertainty in disruption outcomes. In contrast, deflection is a gradual process for adjusting the trajectory of an incoming NEO. Although subcatastrophic impacts such as DART produce significant ejecta (Graykowski et al., 2023; Jewitt et al., 2023; Moreno et al., 2023; Roth et al., 2023), the observed sizes of the ejected fragments are significantly smaller compared to disruption events mainly because of the sensitivities of telescopes observing such fragments. While these definitions distinguish between different outcomes, they also form a continuum within kinetic impactor technology and one spacecraft can achieve either outcome.

The deflection efficiency of a kinetic impactor depends on the target material properties and structure (Raducan et al., 2020; Raducan et al., 2019; Raducan & Jutzi, 2022), and it can be quantified in terms of a momentum enhancement factor, β . β is defined by the momentum balance of the kinetic impact (Cheng et al., 2023),

$$M\Delta\mathbf{v} = m\mathbf{U} + m(\beta - 1)(\hat{\mathbf{E}} \cdot \mathbf{U})\hat{\mathbf{E}} \quad (4)$$

where M is the mass of the asteroid, \mathbf{U} is the impact velocity relative to the asteroid and $\hat{\mathbf{E}}$ is the net ejecta direction. The ejecta produced by the impact can enhance the momentum transfer efficiency. A value of $\beta \approx 1$ would imply that the contribution of ejecta recoil to the momentum transfer was minimal. Conversely, a $\beta > 2$ would indicate that the momentum from the ejecta exceeded that of the incident momentum from the kinetic impactor. For DART, the

observed period change (Thomas et al., 2023) corresponds to a momentum enhancement factor, β , between 2.2 and 4.9, depending on the mass of Dimorphos (Cheng et al., 2023).

For an asteroid of a given size, the momentum enhancement (β) and the catastrophic disruption threshold (Q_D^*) are anti-correlated. Figure 4 shows β values derived by Raducan et al. (2023), as a function of Q_D^* (from this study) for Dimorphos-sized ellipsoidal targets, with different boulder packing. The calculated β values are for the DART impact conditions (580 kg at 6 km/s) and take into account the impact angle and impact location. Impacts on a target with a different curvature may result in a different β value (Hirabayashi et al., 2024), however, the same trends are expected. We find that a target with no large boulders (0 vol% packing) results in a large deflection (large β), however, it is also easier to catastrophically disrupt. On the other hand, for a target with a high boulder packing (50 vol%), β is reduced due to armouring and boulder interlocking (Raducan et al., 2023), and the asteroid is also significantly harder to catastrophically disrupt compared to a target with a low boulder packing.

These findings imply that a greater momentum is necessary for an asteroid with a high Q_D^* to achieve the desired deflection (Δv). Therefore, deflecting an asteroid with a high boulder packing would require a larger and/or faster kinetic impactor. On the other hand, in the case of an asteroid with a low Q_D^* , smaller impactors are preferable due to the heightened risk of disrupting the asteroid. Additionally, with a high β , less spacecraft momentum is needed to attain the desired Δv . When it comes to smaller asteroids, accurately assessing their response to impacts becomes paramount. Q_D^* becomes particularly critical, and its reliance on size underscores the need for precision in predictions. For such cases, the deflection approach must be tailored to the specific characteristics of the target asteroid. In the scenarios where the warning time is sufficiently long, a reconnaissance mission emerges as a prudent choice. This mission may incorporate a small impactor as part of its payload. This approach serves a dual purpose: not only does it offer an opportunity to assess the asteroid’s impact response firsthand, but it also facilitates the estimation of crucial parameters like β and Q_D^* . These assessments inform the deflection strategy. The deflection strategy for small asteroids is contingent on the anticipated response to impacts and can take several forms. Multiple small impacts may be employed, each contributing incrementally to the overall deflection. Alternatively, a single large high-energy impactor may be deployed, delivering a substantial momentum transfer. In more extreme cases, disruption may be the chosen method, potentially resulting in the fragmentation of the asteroid.

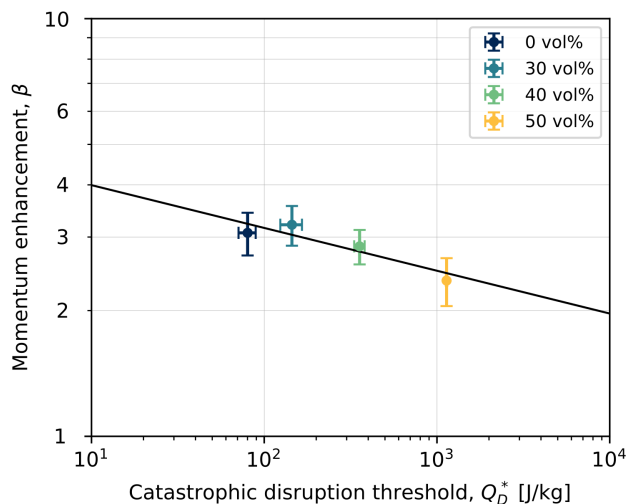


Figure 4: Momentum enhancement, β (from Raducan et al. (2023)) and the catastrophic disruption threshold, Q_D^* (this study) for Dimorphos-sized ellipsoidal targets, with boulder packing between 0 vol% and 50%. β is calculated from numerical simulations using the DART impact conditions (580 kg at 6 km/s) (Raducan et al., 2023). The observed change in the orbital period of Dimorphos, of ≈ 33 minutes (Thomas et al., 2023), corresponds to $\beta = 2.2$ to 4.9, depending on the mass of the asteroid, which is still uncertain.

The highest risk of impacting Earth is posed by asteroids in the ≈ 20 to ≈ 90 meters diameter range. However, a

mission aimed at testing the deflection strategies of near-Earth asteroids in this size range has yet to be undertaken. The impact of a kinetic impactor, similar to DART in both size and velocity at 6 km/s, may catastrophically disrupt an asteroid smaller than approximately 80 meters in diameter. As we continue to refine our deflection strategies, it becomes increasingly clear that any future missions must take the possibility of disruption into account, unless this outcome is expressly intended. This strategic foresight ensures that our efforts to defend against potential asteroid threats are both targeted and effective.

6.2 Implications for the evolution of small asteroids

Our investigation of the disruption threshold for various interior structures within rubble-pile asteroids shows that the catastrophic disruption threshold, Q_D^* , varies significantly contingent upon the boulder packing. In comparison with monolithic targets, Q_D^* of rubble-pile targets is notably smaller for $R < 40$ m and considerably larger for $R > 80$ m. These findings not only bear consequences for planetary defence strategies, influencing how we may redirect or disrupt potential Earth-threatening asteroids but also affect our understanding of the age and structural evolution of rubble-pile asteroids.

Our findings indicate that small rubble-pile asteroids (with radii R less than a few tens of meters) would withstand far fewer and less energetic collisions than their monolithic counterparts. Consequently, the collisional lifetime of rubble-pile asteroids in this size range is less than previously estimated by Bottke et al. (2020) (Fig. 3). This conclusion opens up the possibility of a broader spectrum in the composition of the small asteroid population, suggesting it may include both younger rubble-pile asteroids, whose lifespans are shorter due to their susceptibility to collisions, and older, more resilient monolithic asteroids.

On the other hand, rubble-pile asteroids in the hundred of metre range (e.g., asteroids Dimorphos, Itokawa, Ryugu, Bennu) may be much older. We note that here we call “age” the period of time that has passed since the last disruption event (i.e., it corresponds to the ‘collisional lifetime’). The age of the surface (i.e., the time since the last resurfacing event) may be much younger, as shown in Raducan & Jutzi (2022).

These new Q_D^* trends found in this study could aid in interpreting the cratering record on these small asteroids and their relative ages, shedding new light on the dynamics and evolution of these bodies. This newfound insight calls for a re-evaluation of asteroid evolution models (e.g., Bottke et al., 2020), potentially adjusting the estimated lifetimes of small bodies in the asteroid belt and elsewhere in the Solar System.

7 Conclusions

We used the Bern SPH code to numerically model impact events into small, less than 150 m in diameter, rubble-pile asteroids, with varying boulder packing (between 0 and 50 vol%). In our models, we used the insight gained from the DART impact on asteroid Dimorphos to calibrate the mechanical properties of the target material. Our findings highlight the important role of the interior structure in determining the impact’s outcome and whether it leads to a subcatastrophic or catastrophic event. The same impact energy can catastrophically disrupt a target with a low boulder packing ($\lesssim 30$ vol%), while ejecting only a few percent of material from a target of the same mass, but high boulder packing ($\gtrsim 40$ vol%).

We find that in the case of 50 m in diameter asteroids the catastrophic disruption threshold, Q_D^* can be up to 20 times lower for rubble piles in comparison to monolithic targets. At the same time, targets larger than 160 m in diameter can require up to 3.5 times more energy to disrupt them, compared to monolithic targets.

Our simulations indicate that a DART-sized spacecraft, at 6 km/s possesses the potential to cause catastrophic disruption in rubble-pile asteroids smaller than approximately 80 meters in diameter. Consequently, it is important for future deflection missions to carefully consider the potential for disruption, unless such an outcome is deliberately intended. Our result also implies that asteroids with diameters $\lesssim 50$ m may be much younger than previously predicted while larger asteroids may be much older.

8 Acknowledgements

SDR and MJ acknowledge support from the Swiss National Science Foundation (project number 200021_207359). This work was supported in part by the DART mission, NASA Contract #80MSFC20D0004 to JHU/APL. PM acknowledges funding support from ESA and CNES.

References

- Arakawa, M., Okazaki, M., Nakamura, M., et al. 2022, *Icarus*, 373, 114777
- Artemieva, N. A., & Shuvalov, V. V. 2016, *Annual Review of Earth and Planetary Sciences*, 44, 37
- Ballouz, R.-L., Walsh, K. J., Barnouin, O. S., et al. 2020, *Nature*, 1, publisher: Nature Publishing Group
- Barnouin, O., Ballouz, R.-L., Marchi, S., et al. 2023, *Nature Communications*, Submitted
- Benavidez, P. G., Durda, D. D., Enke, B., et al. 2018, *Icarus*, 304, 143
- Benavidez, P. G., Durda, D. D., Enke, B. L., et al. 2012, *ICARUS*, 1
- Benz, W., & Asphaug, E. 1994, *ICARUS*, 107, 98
- . 1995, *Computer Physics Communications*, 87, 253
- . 1999, *Icarus*, 142, 5
- Bottke, W. F., Vokrouhlický, D., Ballouz, R.-L., et al. 2020, *The Astronomical Journal*, 160, 14
- Chabot, N., et al. 2023, *The Planetary Science Journal*, Submitted
- Cheng, A. F., Agrusa, H. F., Barbee, B. W., et al. 2023, *Nature*, 1
- Collins, G. S., Melosh, H. J., & Ivanov, B. A. 2004, *Meteoritics & Planetary Science*, 39, 217
- Daly, R. T., Ernst, C. M., Barnouin, O. S., et al. 2023, *Nature*, 1
- de León, J., Licandro, J., Duffard, R., & Serra-Ricart, M. 2006, *Advances in Space Research*, 37, 178
- Dotto, E., Deshapriya, J., Gai, I., et al. 2023, *Nature*
- Dunn, T. L., Burbine, T. H., Bottke, W. F., & Clark, J. P. 2013, *Icarus*, 222, 273
- Flynn, G. J., Consolmagno, G. J., Brown, P., & Macke, R. J. 2018, *Geochemistry*, 78, 269
- Graykowski, A., Lambert, R. A., Marchis, F., et al. 2023, *Nature*, 1
- Harris, A. W., & Chodas, P. W. 2021, *Icarus*, 365, 114452
- Hirabayashi, M., et al. 2024, *Nature Comm.*, In review
- Holsapple, K. A., & Housen, K. R. 2019, *Planetary and Space Science*, 179, 104724
- Housen, K. R., & Holsapple, K. A. 1990, *Icarus*, 84, 226
- Ieva, S., Epifani, E. M., Perna, D., et al. 2022, *The Planetary Science Journal*, 3, 183, publisher: IOP Publishing
- Jewitt, D., Kim, Y., Li, J., & Mutchler, M. 2023, *The Astrophysical Journal Letters*, 952, L12
- Jutzi, M. 2015, *Planet. Space Sci*, 107, 3
- Jutzi, M., Benz, W., & Michel, P. 2008, *Icarus*, 198, 242
- Jutzi, M., Benz, W., Toliou, A., Morbidelli, A., & Brasser, R. 2017, *Astronomy & Astrophysics*, 597, A61, publisher: EDP Sciences
- Jutzi, M., Michel, P., Benz, W., & Richardson, D. C. 2010, *Icarus*, 207, 54

Jutzi, M., Michel, P., Hiraoka, K., Nakamura, A. M., & Benz, W. 2009, *Icarus*, 201, 802

Jutzi, M., Raducan, S. D., Zhang, Y., Michel, P., & Arakawa, M. 2022, *Nature Communications*, 13, 7134

Leinhardt, Z. M., & Stewart, S. T. 2009, *Icarus*, 199, 542

Li, J.-Y., Hirabayashi, M., Farnham, T. L., et al. 2023, *Nature*, 1

Lundborg, N. 1967, *International Journal of Rock Mechanics and Mining Sciences & Geomechanics Abstracts*, 4, 269

Luther, R., Raducan, S. D., Burger, C., et al. 2022, *The Planetary Science Journal*, 3, 227

McGlaun, J. M., Thompson, S. L., & Elrick, M. G. 1990, *International Journal of Impact Engineering*, 10, 351

Merrill, C. C., Geiger, C. J., Tahsin, A. T. M., Savransky, D., & Peck, M. 2024, *Acta Astronautica*, 214

Michel, P., Küppers, M., Bagatin, A. C., et al. 2022, *The Planetary Science Journal*, 3, 160

Moreno, F., Bagatin, A. C., Tancredi, G., et al. 2023, *The Planetary Science Journal*, 4, 138

Nyffeler, B. 2004, PhD thesis, University of Bern

Ormö, J., Raducan, S. D., Jutzi, M., et al. 2022, *Earth and Planetary Science Letters*, 594, 117713

Pajola, M., Tusberty, F., Lucchetti, A., et al. 2023, *Nature Communications*, Submitted

Popova, O. P., Jenniskens, P., Emel'yanenko, V., et al. 2013, *Science*, 342, 1069

Raducan, S., Jutzi, M., Cheng, A., et al. 2023, *Nature Astronomy*

Raducan, S. D., Davison, T. M., & Collins, G. S. 2020, *Planetary and Space Science*, 104756

Raducan, S. D., Davison, T. M., Luther, R., & Collins, G. S. 2019, *Icarus*, 329, 282

Raducan, S. D., & Jutzi, M. 2022, *The Planetary Science Journal*, 3, 128

Raducan, S. D., Jutzi, M., Zhang, Y., Ormö, J., & Michel, P. 2022, *Astronomy & Astrophysics*, 665, L10

Richardson, D. C., Quinn, T., Stadel, J., & Lake, G. 2000, *Icarus*, 143, 45

Richardson, D. C., Agrusa, H. F., Barbee, B., et al. 2022, *The Planetary Science Journal*, 3, 157

Rivkin, A. S., Chabot, N. L., Stickle, A. M., et al. 2021, *The Planetary Science Journal*, 2, 173

Robin, C., Murdoch, N., Duchene, A., et al. 2023, Submitted

Roth, N. X., Milam, S. N., Remijan, A. J., et al. 2023, *The Planetary Science Journal*, in press

Rumpf, C. M., Mathias, D. L., Wheeler, L. F., et al. 2020, *Acta Astronautica*, 176, 276

Scheeres, D. J., Hartzell, C. M., Sanchez, P., & Swift, M. 2010, *Icarus*, 210, 968

Stickle, A. M., DeCoster, M. E., Burger, C., et al. 2022, *The Planetary Science Journal*, 3, 248

Thomas, C. A., Naidu, S. P., Scheirich, P., et al. 2023, *Nature*, 1

Tillotson, H. J. 1962, General Atomic Report, GA-3216, 141

Walsh, K. J., Richardson, D. C., & Michel, P. 2008, *Nature*, 454, 188

Wang, K., Li, M., Zhou, Q., & Wang, Y. 2023, *Advances in Space Research*, doi:10.1016/j.asr.2023.06.034

A Supplementary

Table 3: Table of results from Bern SPH simulations of vertical impacts at 6 km/s into ≈ 150 m in diameter rubble pile targets.

R_t^* (m)	Target		Impactor				Fraction remaining (%)
	Packing	M_t (kg)	R_p (m)	M_p (kg)	$E_{kin}/E_{kin(DART)}$	Qr (J/kg)	
75.82	0 vol%	3.25×10^9	0.62	9.76×10^2	1.59	5.41	96.15%
			0.78	1.94×10^3	3.16	10.74	92.18%
			1.06	4.88×10^3	7.94	27.03	82.81%
			1.24	7.81×10^3	12.71	43.26	71.46%
			1.42	1.17×10^4	19.08	64.80	61.89%
			1.84	2.51×10^4	40.92	139.01	13.13%
75.83	30 vol%	3.91×10^9	0.62	9.76×10^2	1.59	4.49	97.68%
			0.78	1.94×10^3	3.16	8.93	95.19%
			1.06	4.88×10^3	7.94	22.47	85.94%
			1.24	7.81×10^3	12.71	35.95	74.83%
			1.42	1.17×10^4	19.08	53.86	66.05%
			1.84	2.51×10^4	40.92	115.55	41.09%
75.91	40 vol%	4.25×10^9	0.62	9.76×10^2	1.59	4.13	99.55%
			0.78	1.94×10^3	3.16	8.22	99.31%
			1.06	4.88×10^3	7.94	20.67	98.85%
			1.24	7.81×10^3	12.71	33.08	98.34%
			1.42	1.17×10^4	19.08	49.55	96.38%
			1.84	2.51×10^4	40.92	106.30	94.75%
			2.44	5.88×10^4	95.67	249.03	79.49%
			2.84	9.27×10^4	150.86	392.59	33.33%
75.92	50 vol%	4.38×10^9	3.12	1.23×10^5	200.03	520.91	1.53%
			0.62	9.76×10^2	1.59	4.01	99.93%
			0.78	1.94×10^3	3.16	7.97	99.84%
			1.06	4.88×10^3	7.94	20.05	99.48%
			1.24	7.81×10^3	12.71	32.10	99.32%
			1.42	1.17×10^4	19.08	48.08	98.55%
			1.84	2.51×10^4	40.92	103.15	97.46%
			2.84	9.27×10^4	150.86	380.94	94.51%
			3.62	1.92×10^5	315.42	788.97	69.68%
			4.42	3.50×10^4	568.70	1487.43	26.05%

*Volume-equivalent target radius.

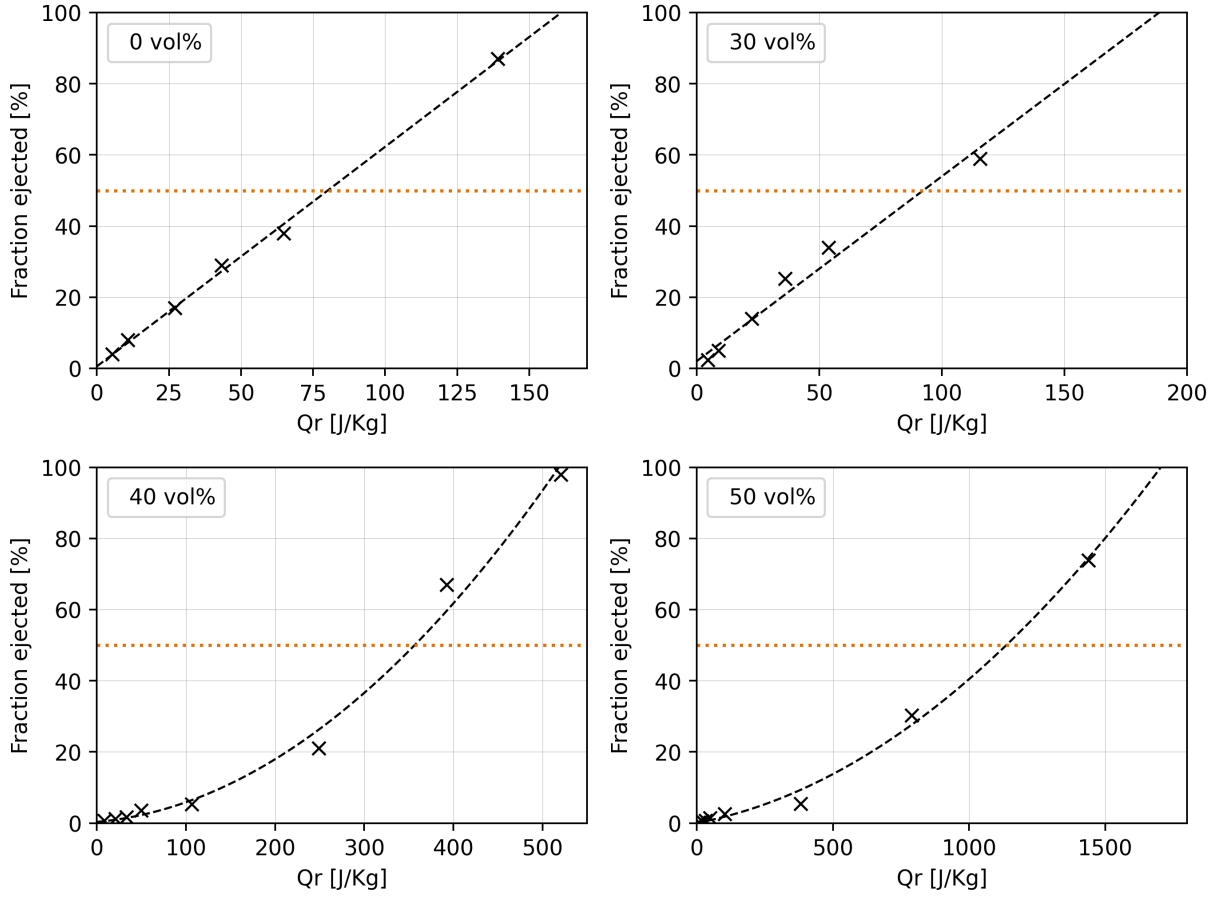


Figure 5: Fraction of ejected material as a function of specific impact energy (Q_r), for 6 km/s impacts into ≈ 150 m rubble pile asteroids with varying boulder packing (0 to 50 %). The intersection between the trend through the simulation data (denoted by the dashed lines) and the 50% fraction ejected (denoted by the dotted lines) denotes the Q_D^* for the specific target.

Table 4: Table of results from Bern SPH simulations of oblique, 45 degrees impacts at 6 km/s into ≈ 150 m in diameter rubble pile targets.

R_t^* (m)	Target		R_p (m)	M_p (kg)	Impactor		Fraction remaining (%)
	Packing	M_t (kg)			$E_{kin}/E_{kin(DART)}$	Qr (J/kg)	
75.82	0 vol%	3.25×10^9	1.42	1.17×10^4	19.3	64.80	76.19%
			1.84	2.51×10^4	41.4	139.01	55.29%
			2.44	5.88×10^4	96.5	325.65	20.12%
75.83	30 vol%	3.91×10^9	1.42	1.17×10^4	19.3	53.86	83.64%
			1.84	2.51×10^4	41.4	115.55	64.02%
			2.44	5.88×10^4	96.5	270.68	38.57%
75.91	40 vol%	4.25×10^9	2.44	5.88×10^4	96.4	249.03	88.40%
			2.84	9.27×10^4	152.6	392.59	63.33%
			3.12	1.23×10^4	202.3	520.91	41.26%
75.92	50 vol%	4.38×10^9	2.84	9.27×10^4	152.6	380.94	78.40%
			4.42	3.50×10^4	575.1	1436.20	40.01%
			4.92	4.82×10^4	793.2	1980.39	11.87%

*Volume-equivalent target radius.

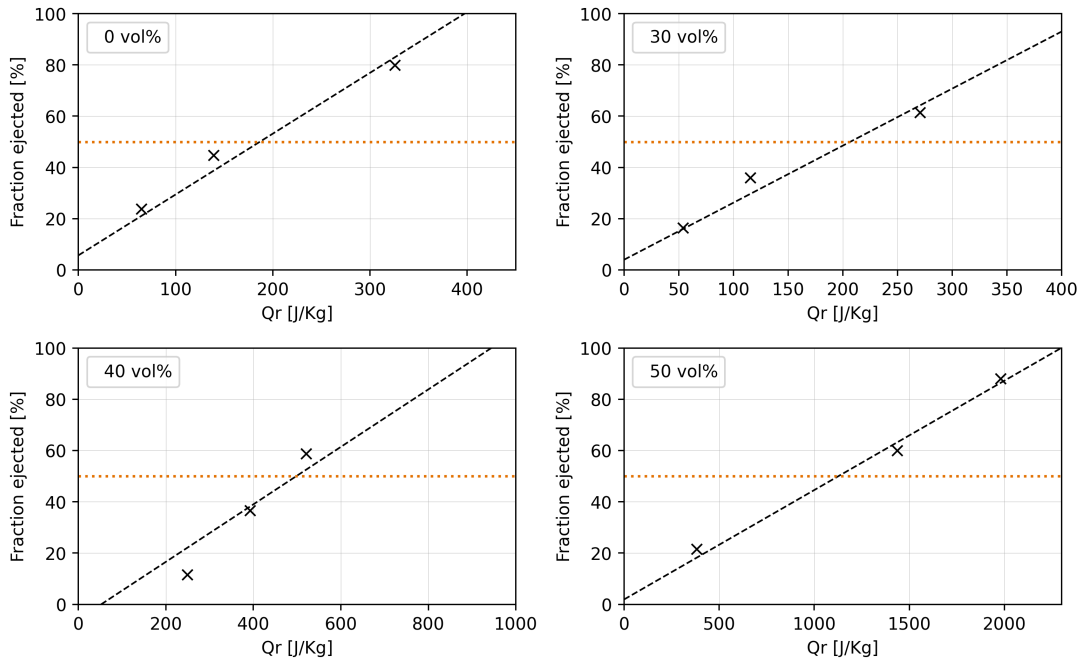


Figure 6: Same as in Fig. 5 but for oblique (45 degrees), 6 km/s impacts into ≈ 150 m rubble pile asteroids with varying boulder packing (0 to 50 %).

Table 5: Table of results from Bern SPH simulations of vertical impacts at 6 km/s into ≈ 100 m in diameter rubble pile targets.

R_t^* (m)	Target		R_p (m)	M_p (kg)	Impactor		Fraction remaining (%)
	Packing	M_t (kg)			$E_{kin}/E_{kin(DART)}$	Qr (J/kg)	
50.57	0 vol%	9.64×10^8	0.78	1.94×10^3	3.20	36.22	79.94%
			1.06	4.88×10^3	8.03	91.42	35.75%
50.58	30 vol%	1.16×10^9	1.06	4.88×10^3	8.03	75.72	69.87%
			1.24	7.81×10^3	12.85	121.19	45.54%
50.75	40 vol%	1.27×10^9	1.06	4.88×10^3	8.03	69.16	87.97%
			1.42	1.17×10^4	19.25	165.82	36.27%
50.90	50 vol%	1.32×10^9	1.84	2.51×10^4	41.38	342.26	53.88%
			2.44	5.88×10^4	96.75	801.75	14.87%

*Volume-equivalent target radius.

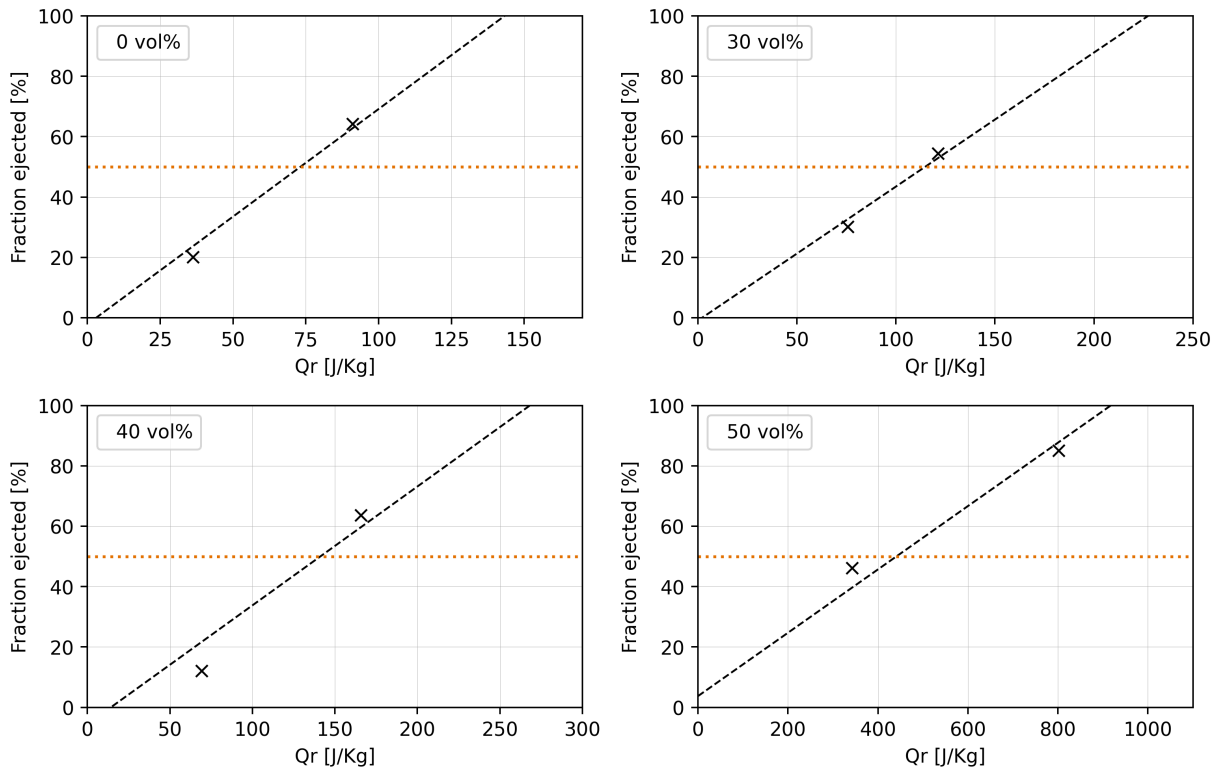


Figure 7: Same as in Fig. 5 but for vertical, 6 km/s impacts into ≈ 110 m rubble pile asteroids with varying boulder packing (0 to 50 %).

Table 6: Table of results from Bern SPH simulations of oblique, 45 degrees impacts at 6 km/s into ≈ 100 m in diameter rubble pile targets.

R_t^* (m)	Target		R_p (m)	M_p (kg)	Impactor		Fraction remaining (%)
	Packing	M_t (kg)			$E_{kin}/E_{kin(DART)}$	Qr (J/kg)	
55.57	0 vol%	9.64×10^8	0.78	1.94×10^3	3.20	36.22	72.62%
			1.06	4.88×10^3	8.03	91.42	47.60%
			1.42	1.17×10^4	19.30	218.46	11.56%
55.58	30 vol%	1.16×10^9	0.78	1.94×10^3	3.20	30.13	83.01%
			1.06	4.88×10^3	8.03	75.72	61.73%
			1.42	1.17×10^4	19.30	181.55	17.57%
55.74	40 vol%	1.27×10^9	1.06	4.88×10^3	8.03	69.16	98.05%
			1.42	1.17×10^4	19.25	165.82	77.58%
			1.84	2.51×10^4	41.38	355.73	17.57%
55.90	50 vol%	1.32×10^9	1.06	4.88×10^3	8.03	342.26	98.64%
			1.42	1.17×10^4	19.30	159.54	88.05%
			1.84	2.51×10^4	41.38	342.26	59.42%

*Volume-equivalent target radius.

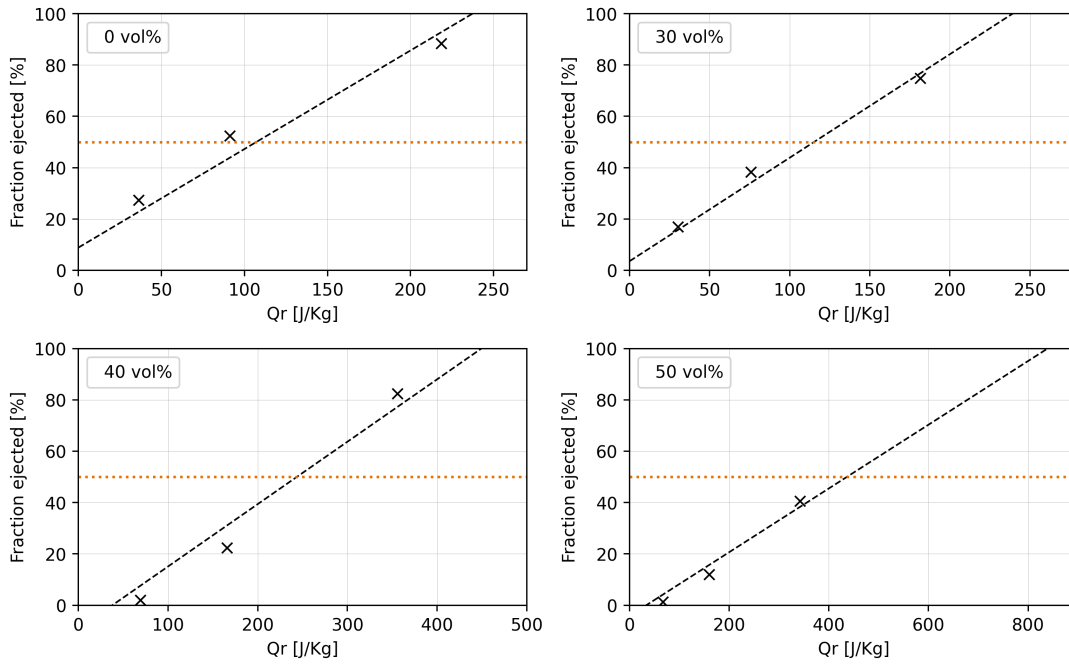


Figure 8: Same as in Fig. 5 but for oblique (45 degrees), 6 km/s impacts into ≈ 100 m rubble pile asteroids with varying boulder packing (0 to 50 %).

Table 7: Table of results from Bern SPH simulations of vertical impacts at 6 km/s into ≈ 50 m in diameter rubble pile targets.

R_t^* (m)	Target		R_p (m)	M_p (kg)	Impactor		Fraction remaining (%)
	Packing	M_t (kg)			$E_{kin}/E_{kin(DART)}$	Qr (J/kg)	
25.32	0 vol%	1.21×10^8	0.36	1.79×10^2	0.29	26.67	44.12%
			0.42	2.84×10^2	0.46	42.35	21.39%
			0.48	4.25×10^2	0.69	63.22	0.30%
25.63	30 vol%	1.51×10^8	0.36	1.79×10^2	0.29	21.37	73.92%
			0.42	2.84×10^2	0.46	33.93	42.24%
			0.48	4.25×10^2	0.69	50.66	18.93%
25.80	40 vol%	1.67×10^8	0.42	2.84×10^2	0.46	30.68	64.95%
			0.54	6.05×10^2	0.98	65.21	19.24%
25.81	50 vol%	1.72×10^8	0.42	2.84×10^2	0.46	29.79	92.86%
			0.54	6.05×10^2	0.98	63.31	49.17%

*Volume-equivalent target radius.

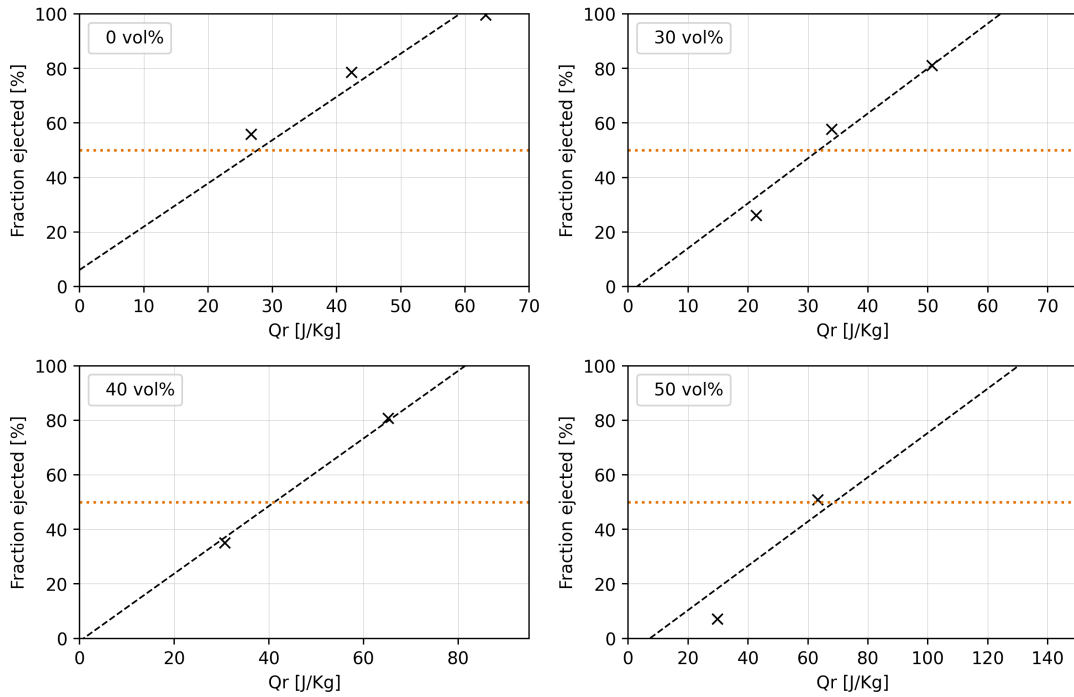


Figure 9: Same as in Fig. 5 but for vertical, 6 km/s impacts into ≈ 50 m rubble pile asteroids with varying boulder packing (0 to 50 %).

Table 8: Table of results from Bern SPH simulations of oblique, 45 degrees impacts at 6 km/s into ≈ 50 m in diameter rubble pile targets.

R_t^* (m)	Target		R_p (m)	M_p (kg)	Impactor		Fraction (%) remaining
	Packing	M_t (kg)			$E_{kin}/E_{kin(DART)}$	Qr (J/kg)	
25.32	0 vol%	1.21×10^8	0.42	2.84×10^2	0.46	42.35	41.52%
			0.54	4.25×10^2	0.69	89.99	13.47%
25.63	30 vol%	1.51×10^8	0.42	2.84×10^2	0.46	33.93	54.06%
			0.54	4.25×10^2	0.69	72.12	33.13%
25.80	40 vol%	1.67×10^8	0.42	2.84×10^2	0.46	30.68	68.73%
			0.54	6.05×10^2	0.98	65.21	36.92%
25.81	50 vol%	1.72×10^8	0.42	2.84×10^2	0.46	29.79	94.68%
			0.54	6.05×10^2	0.98	63.31	52.02%

*Volume-equivalent target radius.

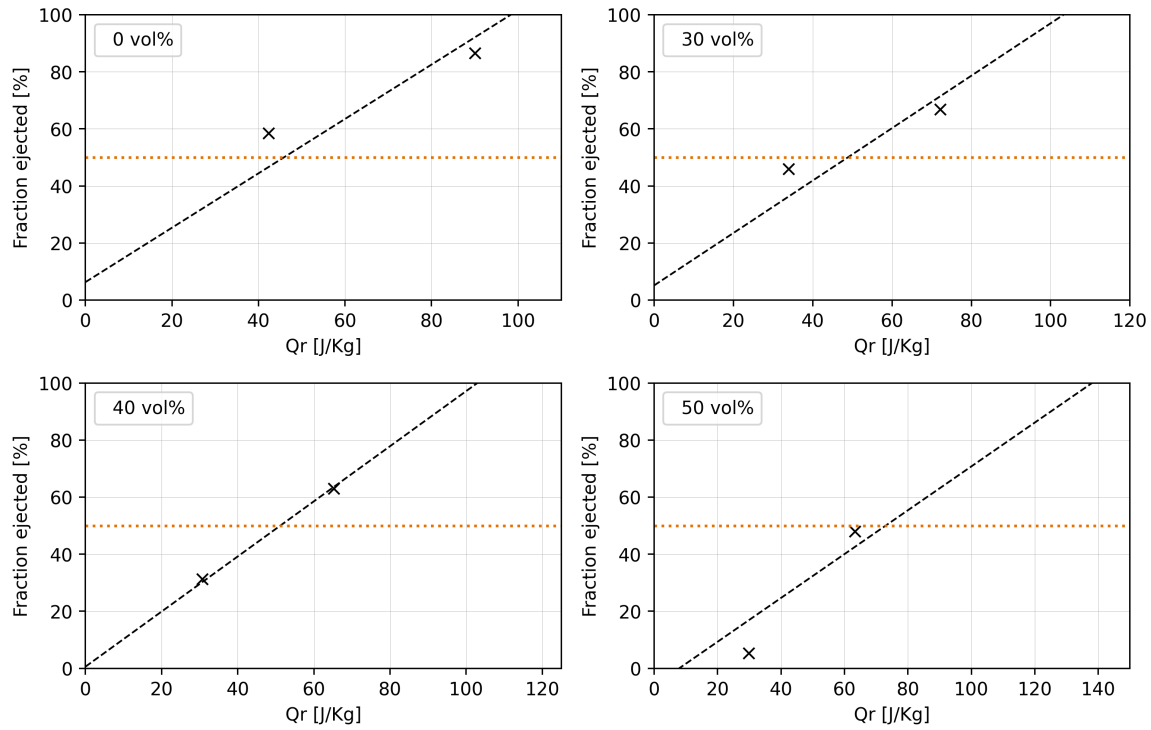


Figure 10: Same as in Fig. 5 but for 45°, 6 km/s impacts into ≈ 50 m rubble pile asteroids with varying boulder packing (0 to 50 %).